Transformation of odor selectivity from projection neurons to single mushroom body neurons mapped with dual-color calcium imaging

Hao Li[a,b], Yiming Li[a,b], Zhengchang Lei[a,b], Kaiyu Wang[a], and Aike Guo[a,c,1]

[a]Institute of Neuroscience and State Key Laboratory of Neuroscience, Shanghai Institutes for Biological Sciences, Chinese Academy of Sciences, Shanghai 200031, China; [b]University of Chinese Academy of Sciences, Shanghai 200031, China; and [c]State Key Laboratory of Brain and Cognitive Science, Institute of Biophysics, Chinese Academy of Sciences, Beijing 100101, China

Edited* by Mu-ming Poo, University of California, Berkeley, CA, and approved June 4, 2013 (received for review April 1, 2013)

Although the response properties of most neurons are, to a large extent, determined by the presynaptic inputs that they receive, comprehensive functional characterization of the presynaptic inputs of a single neuron remains elusive. Toward this goal, we introduce a dual-color calcium imaging approach that simultaneously monitors the responses of a single postsynaptic neuron together with its presynaptic axon terminal inputs in vivo. As a model system, we applied the strategy to the feed-forward connections from the projection neurons (PNs) to the Kenyon cells (KCs) in the mushroom body of *Drosophila* and functionally mapped essentially all PN inputs for some of the KCs. We found that the output of single KCs could be well predicted by a linear summation of the PN input signals, indicating that excitatory PN inputs play the major role in generating odor-selective responses in KCs. When odors failed to activate KC output, local calcium transients restricted to individual postsynaptic sites could be observed in the KC dendrites. The response amplitudes of the local transients often correlated linearly with the presynaptic response amplitudes, allowing direct assay of the strength of single synaptic sites. Furthermore, we found a scaling relationship between the total number of PN terminals that a single KC received and the average synaptic strength of these PN-KC synapses. Our strategy provides a unique perspective on the process of information transmission and integration in a model neural circuit and may be broadly applicable for the study of the origin of neuronal response properties.

G-CaMP | R-GECO | EM reconstruction | functional connectome | inputome mapping

Neurons exhibit a wide variety of response properties that are essential for their functions in the brain. For example, visual cortical neurons are tuned to specific features in the visual stimuli (1), and hippocampal neurons can be tuned to spatial locations in the environment (2) or even to abstract concepts in humans (3). A central problem of systems neuroscience is to elucidate the principles of circuit organization and neuronal computation underlying the generation of such response properties. Because a typical neuron is an integration device that converts many inputs to an output, its response properties are necessarily computed from the response properties of the presynaptic inputs that it receives. Therefore, comprehensive functional mapping of the presynaptic inputs of single neurons should contribute significantly to the questions of the origin of neuronal response properties. Although several previous works (4–8) have made significant advances toward this goal using optical imaging, electron microscopic (EM) reconstruction, or correlative pre- and postsynaptic electrophysiological recording, only a minority of inputs were characterized in these studies, and a comprehensive mapping of the presynaptic inputs to a single neuron remains elusive.

The mushroom body (MB) of *Drosophila*, generally regarded as the third layer of the olfactory pathway, has been extensively studied as a model sensory system (9, 10) (Fig. 1*A*). A particularly well studied area is the MB calyx, where the intrinsic neurons of the MB, the Kenyon cells (KCs), receive inputs from the axon terminals of the projection neurons (PNs). Neural circuitry of the MB calyx offers particular technical advantages for the comprehensive mapping of synaptic connectivity because a single KC receives only a small number of PN inputs and the connections between PNs and KCs form characteristic structures that are within the resolving power of light microscopy (11, 12). Despite the relatively simple circuit structure, a major transformation of odor-evoked response patterns was observed between PNs and KCs, in that single KCs are highly selective for particular odors (13–15), whereas PNs are more broadly tuned (16, 17). This response property of KCs was thought to be functionally important because the MB is widely regarded as a storage center for olfactory memory (10, 18), and KCs with a high level of odor selectivity might minimize the interference between different memories.

A number of hypotheses have been proposed to explain the origin of odor selectivity in KCs. For example, previous studies have suggested that a high level of odor selectivity could be achieved by summing inputs from a large number of randomly selected PNs, followed by thresholding at a high level (19, 20). Temporal patterning of PN inputs relative to the phase of membrane potential oscillations in KCs may also play an important role, based on studies of the locust MB (21). Other works have explored the possible contributions of feed-forward inhibition, intrinsic properties of KCs, and plasticity of PN-KC synapses (22–24). However, experimental support for these ideas has been mostly indirect, and the synaptic origin of odor-evoked responses in KCs remains unclear in *Drosophila*.

Here we investigated this question by comprehensive functional mapping of PN inputs to single KCs. For all of the PN-KC synaptic sites, we simultaneously measured pre- and postsynaptic odor-evoked responses with dual-color calcium imaging. We found that KC output could be well predicted by thresholding the sum of excitatory PN inputs without considering inhibitory inputs, directly supporting the notion that the functional connectivity between PNs and KCs plays a primary role in the generation of highly selective odor responses in KCs. In addition, local calcium transients that likely correspond to subthreshold synaptic activation could be readily observed at postsynaptic sites, opening possibilities for the direct measurement of synaptic transmission and plasticity in this system.

Results

General Strategy. Our strategy for the functional mapping of the presynaptic inputs received by a single postsynaptic neuron is

Author contributions: H.L. and A.G. designed research; H.L. and Y.L. performed research; Z.L. and K.W. contributed new reagents/analytic tools; H.L. and Y.L. analyzed data; and H.L. and A.G. wrote the paper.

The authors declare no conflict of interest.

*This Direct Submission article had a prearranged editor.

[1]To whom correspondence should be addressed. E-mail: akguo@ion.ac.cn.

This article contains supporting information online at www.pnas.org/lookup/suppl/doi:10.1073/pnas.1305857110/-/DCSupplemental.

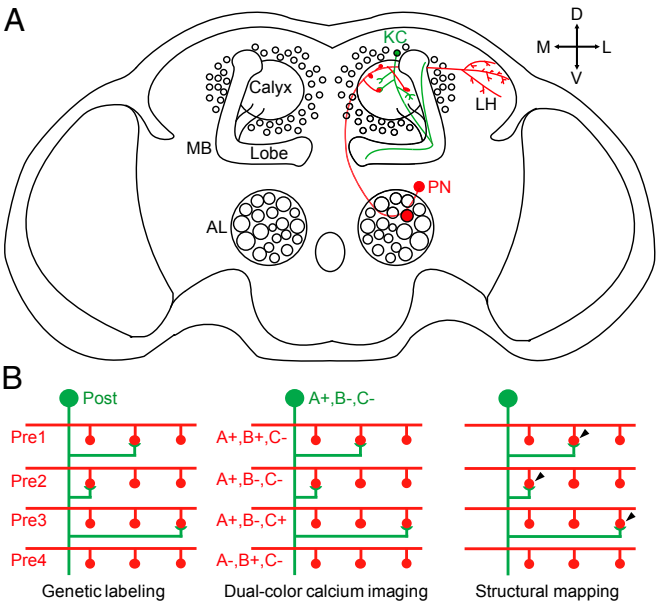

Fig. 1. Illustrations of the MB calyx and the mapping strategy. (*A*) Structure of the MB calyx and its location in the *Drosophila* brain. The shape of a typical PN is shown in red and a typical KC is shown in green. AL, antennal lobe; MB, mushroom body; LH, lateral horn; PN, projection neuron; KC, Kenyon cell; D, dorsal; V, ventral; M, medial; L, lateral. (*B*) Illustration of the mapping strategy. First, neurons are genetically labeled so that a single postsynaptic neuron "post" and all presynaptic neurons "pre" express calcium indicator proteins of different colors (green and red). Dual-color calcium imaging is then used to map the response properties (e.g., to the three stimuli A, B, and C) of the postsynaptic neuron (e.g., responding to stimulus A only, represented as A+, B–, and C–) and all of the presynaptic terminals, regardless of their connectivity. Structural mapping is then carried out to identify the actual sites of synaptic contacts (post with pre 1, 2, and 3), and the presynaptic partners of the single postsynaptic neuron could then be pooled together for analysis. In this illustration, all three presynaptic inputs responded to A whereas only one of them responded to B and C, explaining the response pattern of the postsynaptic neuron.

illustrated in Fig. 1*B*. To implement the strategy in the MB calyx, we sparsely labeled single KCs with genetically targeted expression of the green calcium indicator protein G-CaMP3 (25), while simultaneously densely labeled the presynaptic PNs with the expression of the red calcium indicator protein R-GECO1 (26). The odor-evoked response properties of single KCs and the population of presynaptic PN axon terminals could then be simultaneously measured with dual-color calcium imaging over the entire MB calyx. Afterward, by locating the claw-like structures of KCs that are indicative of synaptic connections (11, 27), the PN axon terminals that made synapses with the single postsynaptic KC could be unambiguously determined and analyzed with light microscopy.

Dual-Color Calcium Imaging. Although G-CaMP3 has been extensively used and calibrated as a neural activity reporter in *Drosophila*, R-GECO1 has not yet been introduced to this model organism. Therefore, we made transgenic flies carrying *UAS-R-GECO1* and calibrated its response characteristics against G-CaMP3 by expressing both *UAS-G-CaMP3* and *UAS-R-GECO1* in the PNs with *GH146-GAL4*. We found that PN axon terminals could be clearly visualized by the basal fluorescence of G-CaMP3 and R-GECO1, with no obvious difference between images obtained from the two channels (Fig. S1*A*). When an odor was presented to the fly in vivo, fluorescence increase in the axon terminals could be detected in both channels with similar activation patterns (Fig. S1*B*). By comparing the odor-evoked signals of the two calcium indicator proteins from individual PN axon terminals (Fig. S1*C*), we found that the peak response amplitude of R-GECO1 is approximately half that of G-CaMP3 and that this relationship is essentially linear across the whole dynamic range (Fig. S1*D*). The temporal kinetics of calcium responses recorded by R-GECO1 is also comparable to that of G-CaMP3 (Fig. S1*C*), showing similar time constants during the decay phase of the odor-evoked calcium transients (Fig. S1*E*). Therefore, R-GECO1 and G-CaMP3 compose a pair of indicators with similar calcium response properties, except that their response amplitudes differ by approximately twofold.

Structural Mapping of PN Axon Terminals to Single KCs. We used a FLP (flippase)-out strategy (28) to stochastically drive *UAS-G-CaMP3* expression in single KCs from the ~2,000 KCs covered by *OK107-GAL4* (29). Simultaneously, we used *GH146-QF* to drive *QUAS-R-GECO1* expression in ~90 PNs, covering more than half of the PN population (30). Although *GH146-QF* does not cover all of the PNs, single KCs connect with only a small number of PN terminals, and we show below that complete or semicomplete mapping of PN inputs could be found for a substantial number of the randomly labeled KCs. Under light microscopy, the MB calyx was clearly outlined by the surrounding glial cells (Fig. 2 *A–C* and Movie S1), which were fluorescent because of a transgenic element carried in *GH146-QF* (30).

Of the 263 MB calyces analyzed, G-CaMP3 expression in single KCs or clones of KCs could be detected in 176 calyces with 2.6 ± 2.1 (mean ± SD, as for all values below) KCs labeled per calyx. The KCs are unipolar neurons with simple and stereotyped dendrites that are highly amendable to analysis (Fig. 2 *C–E*) (11, 12, 31). After leaving the cell body, the main process of a KC sent out 3.2 ± 1.5 primary side branches in the MB calyx ($n = 23$, Fig. 2*F*) before being collected into a bundle that extended anteriorly to become the axonal lobes (Fig. 1*A*). More than half of the primary branches (57 ± 27%, $n = 23$) gave rise to a small number of secondary branches (1.6 ± 0.9, $n = 39$, Fig. 2*G*), but tertiary branches were rarely found from secondary branches (4 of 62). Most of the branches ended with a claw-like structure that encircled a single PN axon terminal; these were exceptionally large globular structures that often extended to more than 2 μm (Fig. 2*E*). Counting from all of the branches, the total number of claws per KC was 6.2 ± 2.4 ($n = 23$, Fig. 2*H*). On average, for more than half of the claws (61 ± 26%, $n = 23$, Fig. 2*I*), the presynaptic PN axon terminals encircled by the claws were found to express R-GECO1. No structure was visible inside the other claws, likely because the corresponding PN axon terminals did not express *GH146-QF* because these axon terminals could be revealed by immunostaining for choline acetyltransferase (ChAT) (Fig. 2*E*). Notably, for more than 15% of the single KCs, essentially all of the PN terminals (>90%) encircled by the claws were covered by R-GECO1 (Fig. 2*I*).

EM Analysis of the MB Calyx. Although evidence from previous studies supports the idea that the sites of synaptic contacts between PNs and KCs are restricted to the claw-like endings of KC dendritic branches (11, 27), a rigorous examination of this hypothesis requires extensive reconstructions of single KCs at the EM level. Therefore, we reconstructed 3D structures of 59 single KCs from a stack of 450 EM images obtained with focused ion beam scanning electron microscopy (FIB-SEM) (32). The acquired total volume consists of two adjacent cubes of 50 × 50 × 9.4 μm^3 and 26 × 26 × 8.7 μm^3 with voxels of 12.6 × 12.6 × 40 nm^3 and 6.3 × 6.3 × 40 nm^3, respectively. In total, this dataset covered ~20% of one calyx (Fig. 3 *A* and *B*). We identified 85 synaptic contacts between PN axon terminals and KCs, as indicated by established criteria for presynaptic specialization including prominent densities, presence of clustered synaptic vesicles, and T-bar–like structures (Fig. 3*C*; Fig. S2; Table S1; Movie S2) (11, 27). We found that ~85% of the PN-KC synapses (72/85) were made onto KC claws (Fig. 3*D*), ~9% of the synapses (8/85) were made onto the ending of filopodia-like structures on KC dendrites (Fig. 3*E*), and ~6% of the synapses (5/85) were made on

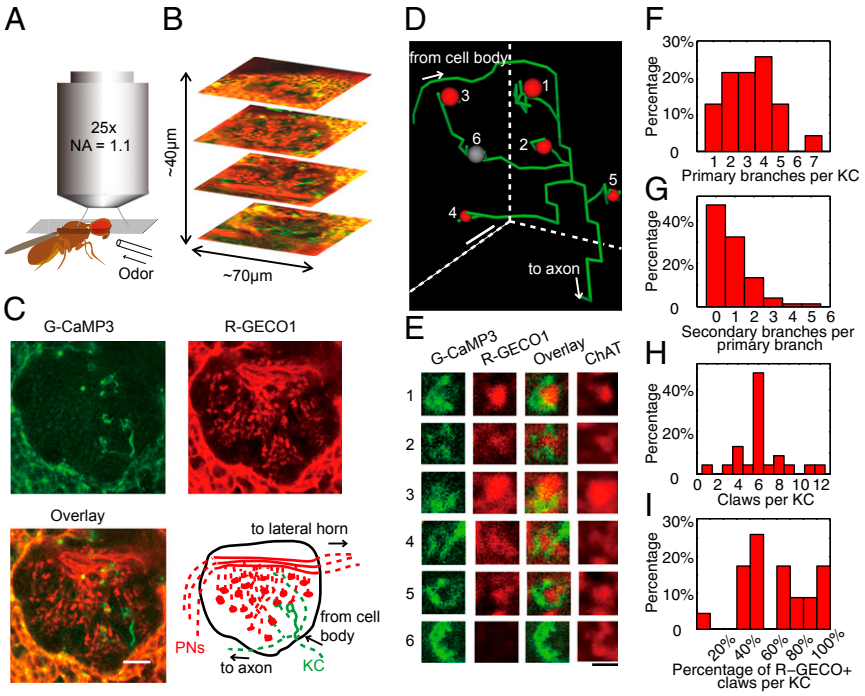

Fig. 2. Mapping the presynaptic inputs of single KCs. (*A*) Experimental setup for in vivo structural and functional mapping. (*B*) The entire MB calyx was mapped by repeating single-plane imaging along the Z-direction. (*C*) Example structural image of a MB calyx in vivo, in which a single KC expressed G-CaMP3 and many PNs expressed R-GECO1. The complete image stack is shown in Movie S1. Interpretation of the image is shown in the illustration, where dashed lines indicate neurites that were above or below the focus of view. (*D* and *E*) Based on the structural images, the 3D structure of the entire KC dendrite was traced, and all of the KC claws were numbered and inspected to locate the corresponding PN axon terminals (first three columns in *E*). For this KC, five of the claws (except row 6) encircled PN axon terminals expressing R-GECO1. The PN axon terminal encircled by claw no. 6 could be revealed after immunostaining (final column in *E*). Diameter of the KC was exaggerated in *D* for illustration. (*F*) Histogram of the number of primary branches per KC. (*G*) Histogram of the number of secondary branches per primary branch. (*H*) Histogram of the number of claws per KC. (*I*) Histogram of the percentage of claws per KC that encircle PN axon terminals expressing R-GECO1. (Scale bars: *C* and *D*, 10 μm; *E*, 3 μm.)

the shaft of KC dendrites (Fig. 3*F*). Furthermore, every KC claw that we identified ($n = 27$) received synapses from the PN axon terminal that it encircled, with an average number of 2.4 synapses per claw. Therefore, the great majority of PN inputs to KCs were made from the PN axon terminals to the KC claws, allowing us to map the PN-KC connections comprehensively by focusing on these structures. The PN inputs that were located on the filopodia or shaft of KCs were not analyzed further because these connections could not be unambiguously identified with light microscopy.

Odor-Evoked Calcium Transients in KCs. Individual PN axon terminals and the dendrites of single KCs could be clearly resolved during functional imaging, revealing differential odor-evoked response patterns (Fig. S3). No significant adaptation effect was found after a few pretrial exposures, enabling us to functionally map the entire calyx by repeating single-plane trials along the *z* axis (Fig. S4). Consistent with previous findings (13, 15), the responses of single KCs was highly selective to particular odors, and each odor activated a small percentage of KCs (Fig. S5). We first studied the odor response patterns of the complete dendritic trees of single KCs in the calyx and found that the calcium transients evoked by odors exhibited heterogeneous spatial patterns (Fig. 4*A*). For 23 KCs that projected to the vertical lobes (18 α/β KCs, 5 α′/β′ KCs), we recorded the response patterns of the KC axon at the tip of the vertical lobe as a readout of KC output and compared them with the response patterns of the dendrites in the calyx. When a positive odor response was found at the KC axon, global calcium transients with large average dendritic response amplitudes could almost always be found covering most of the dendrites (Fig. 4 *A* and *B*), suggesting that these events correspond to suprathreshold activation of KCs. When odors evoked global calcium transients, the amplitudes of calcium signals of the postsynaptic claws did not correlate with those of the corresponding presynaptic terminals (Fig. 4*C*), suggesting high variability in the contribution of individual PN terminals to the KC responses. When an odor evoked no obvious response at the KC axon, global calcium transients were absent from KC dendrites, but local calcium transients restricted around postsynaptic sites were often observed (Fig. 4*A*). The spatial profile of the local calcium transients could be well fitted using Gaussian distributions centered at the claw with an average SD of 4.2 ± 0.8 μm ($n = 23$, Fig. 4 *D* and *E*). These events were invariably accompanied by the activation of the corresponding PN terminals (Fig. 4*F*). For individual claws, the amplitude of the local calcium transients often showed a linear relationship with the amplitude of presynaptic calcium signals (Fig. 4*G*), suggesting that local calcium transients correspond to subthreshold activation of KCs caused by presynaptic PN activation, and that the regression coefficient provides a measure of the effective synaptic strength.

Input–Output Relationship of Single KCs. To investigate the origin of odor selectivity of KCs, we pooled together all identified presynaptic PN inputs of single KCs and compared them with the KC output. As the simplest measure, we first examined whether the arithmetic sum of PN input responses could be useful for predicting KC output. In the example shown in Fig. 5*A*, we identified seven PN terminals, five of which were labeled with R-GECO1, each responding differentially to five different odors. The KC axon showed a detectable response to only one of the odors, which also evoked the highest amplitude of the summed PN inputs (Fig. 5*B*). In 8 of the 10 KCs that responded to at least one odor, the odor that triggered KC output responses also elicited the largest summed inputs ($P < 0.001$, Fig. 5*C*). Thus, the output of single KCs is strongly correlated with the PN inputs that they receive and may be predicted by placing a threshold on the arithmetic sum of PN input responses.

Scaling of Average Synaptic Efficacy with Total Synapse Number on Single KCs. Inspection of Fig. 5*C* showed that the amplitude of the summed PN calcium signals required to activate the KC appeared to increase with the number of PN axon terminals received by the KC. Assuming a constant threshold for KC activation, this finding indicates that the average synaptic strength per PN terminal is scaled down with an increasing number of input PN terminals. To search for a simple scaling rule for the dependence of average PN synaptic strength on the PN terminal number n, we tested two scaling rules in which the summed PN signals were divided by n or by $\log(n)$ and evaluated the improvement of the scaled summed PN signals in predicting KC output. This evaluation was quantitative performed with the

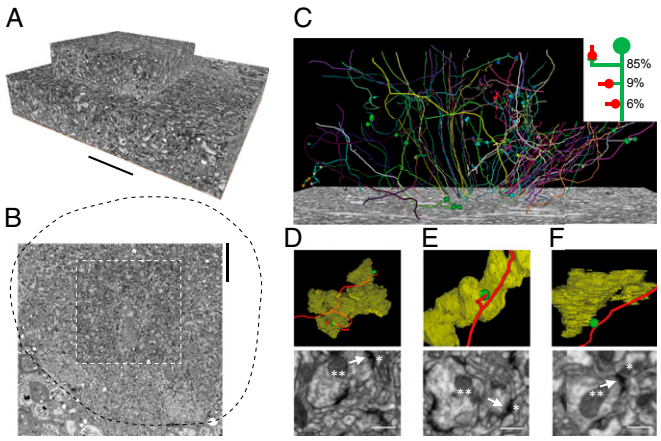

Fig. 3. EM analysis of the MB calyx. (*A*) Total image volume acquired. (*B*) Location of the acquired volume in the calyx. The black dashed line outlines the calyx, and the white dashed line outlines the rectangular area covered by the top cube. (*C*) Three-dimensional structures of 59 reconstructed single KCs. Balls indicate synapses from PN axon terminals to the traced KCs. The synapses can be classified into three types, with their frequencies of occurrence shown in the *Inset*. (*D*–*F*) Synapses from PN axon terminals to KCs that were made onto a claw (*D*), a filopodia-like ending (*E*), and the shaft of a branch (*F*). (*Upper*) Reconstructions of the volume-rendered PN axon terminals (yellow), skeletons of the KCs (red), and locations of synapses (green balls). (*Lower*) The actual EM images for the identification of synapses. A double asterisk indicates a PN axon terminal; a single asterisk indicates a KC; arrows point to synapses. (Scale bars: *A* and *B*, 10 μm; *D*–*F*, 0.5 μm.)

receiver operating characteristics (ROC) curves (Fig. 5*D*). By systematically varying the threshold for classification, the optimal rule that maximized true positives and minimized false positives could be selected. The results showed that scaling by either n or $\log(n)$ improved classification performance (Fig. 5*E*) and that $\log(n)$ provided better improvement with an error rate of ~20% at the optimal operating point. At this point, the threshold of the summed PN signals required for KC activation was $\Sigma(dF/F)_{PN} = 0.71 * \log(n)$.

It is also conceivable that the effective strength of the PN terminals in exciting KC depends on their distance to the axon because of spatial attenuation in the dendrite (33). However, when different PN inputs were weighted according to their distance from the corresponding claw to the axon initial segment (34), we found a decrease rather than an increase in the prediction of KC output by the summed PN inputs (Fig. S6), suggesting that PN terminals exert similar influences on the KC output regardless of their synaptic locations. Taken together, these results showed that selective odor-evoked responses in KCs could be well predicted by a linear summation of the excitatory PN input signals and that the average synaptic strength of PN inputs is scaled with the total number of PN terminals on each KC.

Discussion

In this work, we have developed a strategy for the comprehensive functional mapping of the presynaptic inputs of a single neuron and have applied the strategy to the connections between PNs and KCs in the *Drosophila* olfactory system. Simultaneous dual-color calcium imaging of presynaptic terminals and single postsynaptic neurons allowed us to analyze the relationship between presynaptic activation and postsynaptic response during olfactory processing. We found that the odor selectivity of single KCs could be well predicted by thresholding the arithmetic sum of the presynaptic PN calcium signals, indicating that odor selectivity in KCs is primarily determined by the excitatory PN inputs. Furthermore, we discovered that the average synaptic strength of PN axon terminals on a KC scales with the total number of PN terminals received by the KC.

Origin of Subcellular Calcium Dynamics. The local and global calcium transients that we observed in the KCs are similar to those found previously in the mammalian brain in vivo (6, 7, 35), where local transients reflect synaptic activation and global transients reflect back-propagating action potentials or dendritic spikes. That global calcium transients in KCs are due to back-propagating action potentials is supported by the finding that they are highly correlated with KC axon activation. Cultured KCs express nicotinic cholinergic receptors that are permeable to calcium (36), and it is likely that these receptors contribute to the local calcium transients in KCs. We found that the amplitude of local calcium transients often scaled linearly with the amplitude of presynaptic calcium signals, indicating that the effective strength of single synaptic sites can be estimated with dual-color calcium imaging. Although the limited sensitivity of G-CaMP3 prevented

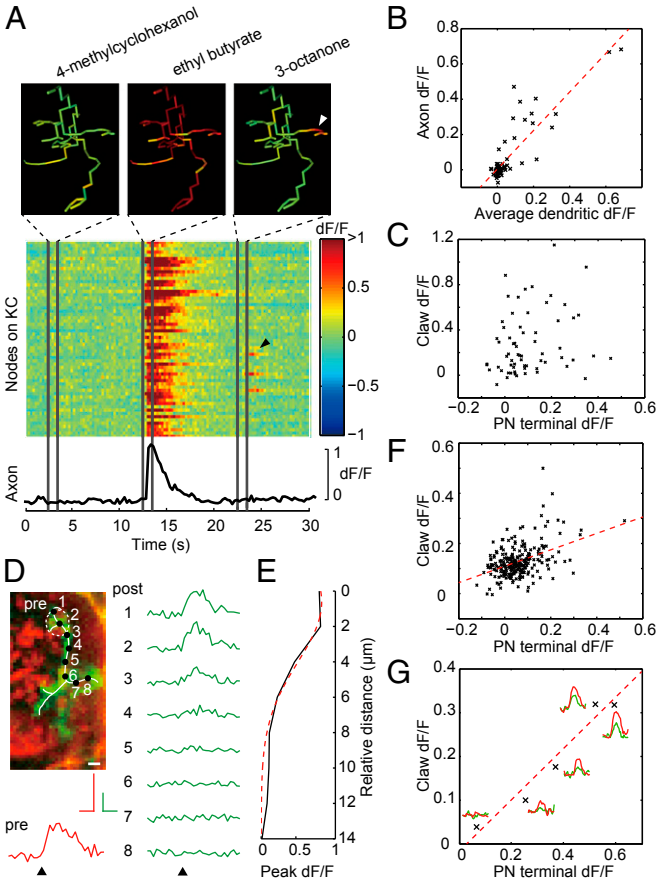

Fig. 4. Odor-evoked calcium transients in single KCs. (*A*) Odor-evoked calcium transients in the dendrite and axon of a KC. Ethyl butyrate evoked global calcium transient in the entire dendritic tree and the axon, whereas 3-octanone evoked a local calcium transient in a single claw, marked by an arrowhead. (*B*) Response at the axon was correlated with the occurrence of global calcium transients as reflected by a large average dendritic response; $n = 85$, $R^2 = 0.76$, $P < 0.001$. (*C*) In the presence of global calcium transients, response amplitude of the KC claws did not correlate significantly with presynaptic PN activation; $n = 65$, $R^2 = 0.03$, $P = 0.07$. (*D*) Local calcium transients were localized to KC claws. Response traces of eight nodes along the dendrite are shown in green, and the response trace of the corresponding PN axon terminal (pre) is shown in red. (*E*) Decay of peak response amplitude along the dendrite shown in *D*, fitted with a Gaussian curve (red dashed line); $R^2 = 0.96$. (*F*) Pre- and postsynaptic response amplitudes were significantly correlated in the absence of global calcium transients; $n = 240$, $R^2 = 0.18$, $P < 0.001$. (*G*) Linear relationship between pre- and postsynaptic response from a single claw; $n = 5$ trials, $R^2 = 0.94$, $P = 0.004$. The actual response traces are shown, with the red traces from the PN axon terminal and the green traces from the claw. (Scale bar in *D*, 2 μm.) 1 s, 50% *dF/F*.

NEUROSCIENCE

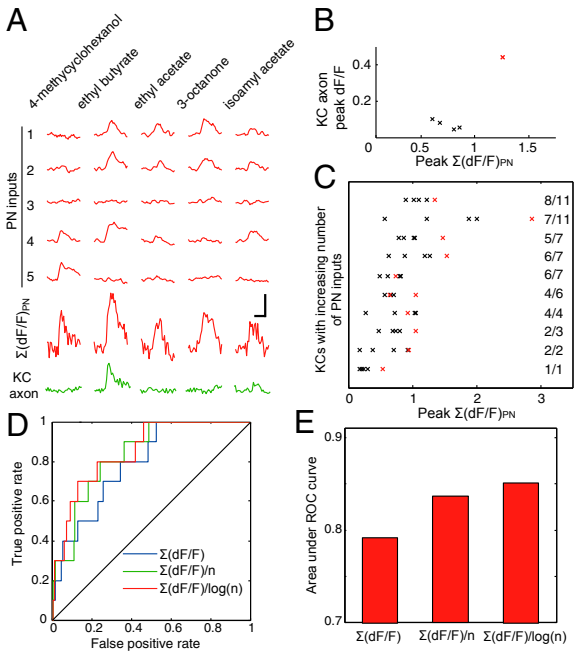

Fig. 5. Predicting the output of single KCs from inputs. (*A*) Odor-evoked responses recorded from the axon and the PN inputs of a single KC. (*B*) Relationship between the response amplitude of the summed PN inputs and the axon output for the KC in *A*, with each cross representing peak response amplitudes evoked by a single odor. The odor (ethyl butyrate) that evoked a significant axon response is in red. (*C*) Relationship between the response amplitude of the summed PN inputs and axon activation for all of the odor-responsive KCs. Crosses in red indicate significant responses at the KC axon. The number at the end of each line indicates the number of PN inputs covered by R-GECO1 divided by the total number of PN inputs. (*D*) ROC curves for binary classifiers based on $\Sigma(dF/F)_{PN}$, $\Sigma(dF/F)_{PN}/n$, and $\Sigma(dF/F)_{PN}/\log(n)$. (*E*) Comparison between the areas under ROC curves. (Scale bars in *A*, 2 s, 50% *dF/F*.)

us from obtaining a comprehensive mapping of effective synaptic strengths for single KCs in this work, new generations of calcium indicator proteins with higher sensitivities promise that such a goal eventually could be achieved (26, 37). Such information should be especially helpful for the understanding of neuronal computation in the MB, a brain area widely regarded as a storage site for olfactory memories (10, 18).

Input Integration in KCs. The integration rule of KCs in *Drosophila* is currently not fully understood. Similar neurons in the locust are known to exhibit strong oscillation of membrane potential upon odor stimulation, a response that may be caused by oscillatory PN input or feedback inhibition in the MB (21, 38, 39). For such neurons, it is likely that the inputs are not linearly summed, and the timing of inputs relative to the phase of oscillation could be important. Although calcium imaging does not easily allow analysis of neural activity at the millisecond scale, the fact that the KC output could be well predicted by the sum of relatively slow calcium signals suggests that fine temporal coding is not essential for the generation of odor responses in this system. This is consistent with previous findings (15) that KCs in *Drosophila*, unlike similar neurons in the locust, do not exhibit strong oscillation of membrane potential upon odor stimulation. The very large input resistance measured from KCs also resulted in a large membrane time constant (15), making it more likely that they function as temporal integrators rather than as coincidence detectors.

Scaling of PN-KC Synaptic Strength. Our analysis of the input–output relationship of single KCs revealed that, under the assumption of a constant firing threshold, the average synaptic strength per PN terminal is scaled down with an increasing number of input PN terminals. In the absence of such a mechanism, KCs that receive larger numbers of PN inputs would be proportionally more likely to be activated by odors than those that receive smaller numbers of PN inputs, resulting in biased representations of odors in the MB. Therefore, scaling of the average strength of PN-KC synapses with the number of PN inputs ensures that KCs with a different number of PN inputs could be activated by odors with similar frequency. The cellular mechanism underlying such synaptic scaling could be intrinsic to KCs, for example, by maintaining a relatively constant pool of postsynaptic transmitter receptors available to PN inputs in all of the KCs. Those KCs with larger numbers of PN inputs would provide fewer postsynaptic receptors for each PN-KC synapse, thereby downscaling average synaptic strength. Alternatively, the number of inhibitory synapses received by a KC may be correlated with the number of excitatory synapses from PNs, so that the efficacy of PN inputs in activating the KC is effectively downregulated.

Toward "Inputome" Mapping for Single KCs. In addition to the excitatory PN inputs, previous works have shown that the MB calyx is also innervated by a small number of GABAergic, octopaminergic, and dopaminergic neurons (40). The inhibitory GABAergic neurons make synaptic contacts with both PN axon terminals and KC dendrites (27). It is possible that the response properties of PN inputs that we have mapped here were already modified by presynaptic inhibition from these neurons. Presynaptic inhibition has been found to be important to gain control at the stage of inputs to PNs (41) and may also play a similar role at the PN-KC connections to control the average output level of PNs. The postsynaptic inhibitory component of KCs may also play a role in determining the effectiveness of postsynaptic activation by the PN inputs through either membrane hyperpolarization or local shunting. A complete mapping of the presynaptic inputs to single KCs that includes the inhibitory and neuromodulatory components—the inputome of single KCs—would undoubtedly further deepen our understanding of the rules of neuronal computation in the MB.

Functional Mapping of Presynaptic Inputs. The strategy that we introduced here rests on two components: dual-color calcium imaging for the simultaneous measurement of pre- and postsynaptic responses and a genetic labeling scheme that allowed us to identify the presynaptic partners of a particular postsynaptic neuron. For the MB calyx, we took advantage of the fact that the sites of PN-KC connections could be reliably identified by claw-like structures that are visible under light microscopy. Specialized axon/dendrite morphology associated with synaptic connections is also found in many other systems, such as the mossy fiber terminals on the granule cells of the cerebellum, where each granule cell forms four or five short dendrites that end in claw-like structures on mossy fiber terminals (42). In the absence of such specialized structures, direct EM reconstruction could be carried out with the help of genetically encoded tags that are visible under both light and electron microscopy (43). Alternatively, methods of monosynaptic retrograde virus tracing may be adapted to label the presynaptic partners of single neurons (44, 45). Although the number of inputs received by KCs is relatively small, with the emerging techniques of fast 3D optical microscopy (46, 47) and high throughput EM (4, 5, 32), it is conceivable that this strategy could be scaled up in the future for the analysis of more complex neural circuits.

Materials and Methods

For full details, see *SI Materials and Methods*.

Transgenic flies carrying *UAS-R-GECO1* or *QUAS-R-GECO1* were generated according to standard procedures. For the generation of FLP-out clones for dual-color calcium imaging, flies of the genotype *tub-FRT-GAL80-FRT/+; QUAS-R-GECO1, QUAS-R-GECO1/UAS-G-CaMP3; GH146-QF/MKRS, hsFLP; OK107-GAL4/+* were heat-shocked at 37 °C for 15 min during

the late pupal stage. These flies were prepared for in vivo calcium imaging by exposing the brain above the recording chamber while keeping the antenna below for odor presentation. Olfactory responses of the PN axon terminals and the single KCs were then imaged by repeating single-plane sessions along the Z-direction to cover the whole calyx. After imaging, brains were processed for immunohistochemical staining against ChAT to facilitate the analysis of structural connectivity based on optical images. Response traces of KCs or PN axon terminals were calculated by averaging the fluorescence level inside regions of interest (ROIs) that were manually traced. To calculate *dF/F* for the response traces, the baseline fluorescence level during the time interval 0–2.5 s before odor onset was averaged and then subtracted and divided from the response trace. Fluorescence level had to be >3.5 SD above the baseline fluorescence level at any time during the time interval 0–2.5 s after odor onset to be counted as a positive response. If a positive response was found, the peak *dF/F* during the time interval 0–2.5 s after odor onset was measured as the response amplitude. Brains for EM analysis were fixed with glutaraldehyde and osmium tetroxide, en bloc-stained with uranium acetate, embedded in Epon, and imaged with FIB-SEM.

ACKNOWLEDGMENTS. We thank Q. Hu, Q. Ma, and Y. Yang [Optical Imaging Facility, Institute of Neuroscience (ION)] for optical imaging support; G. Ji and J. Zhang (Center for Biological Imaging at the Institute of Biophysics) and Y. Kong and L. Wang (Electron Microscopy Facility, ION) for EM support; M. Zhang for electronics and machining support; L. Looger for G-CaMP3 flies; R. Campbell for the R-GECO1 construct; S. Wen for proofreading neuron tracing; K. Scott and the Bloomington Stock Center for providing fly stocks; and M. Poo for critical reading of the manuscript. This work was supported by 973 Program Grant 2011CBA00400 (to A.G.); Natural Science Foundation of China Grants 30921064, 90820008, and 31130027 (to A.G.); and Strategic Priority Research Program of the Chinese Academy of Sciences Grant XDB02040100 (to A.G.).

1. Hubel DH, Wiesel TN (1962) Receptive fields, binocular interaction and functional architecture in the cat's visual cortex. *J Physiol* 160:106–154.
2. O'Keefe J, Dostrovsky J (1971) The hippocampus as a spatial map. Preliminary evidence from unit activity in the freely-moving rat. *Brain Res* 34(1):171–175.
3. Quiroga RQ, Reddy L, Kreiman G, Koch C, Fried I (2005) Invariant visual representation by single neurons in the human brain. *Nature* 435(7045):1102–1107.
4. Bock DD, et al. (2011) Network anatomy and in vivo physiology of visual cortical neurons. *Nature* 471(7337):177–182.
5. Briggman KL, Helmstaedter M, Denk W (2011) Wiring specificity in the direction-selectivity circuit of the retina. *Nature* 471(7337):183–188.
6. Jia H, Rochefort NL, Chen X, Konnerth A (2010) Dendritic organization of sensory input to cortical neurons in vivo. *Nature* 464(7293):1307–1312.
7. Chen X, Leischner U, Rochefort NL, Nelken I, Konnerth A (2011) Functional mapping of single spines in cortical neurons in vivo. *Nature* 475(7357):501–505.
8. Reid RC, Alonso JM (1995) Specificity of monosynaptic connections from thalamus to visual cortex. *Nature* 378(6554):281–284.
9. Masse NY, Turner GC, Jefferis GS (2009) Olfactory information processing in Drosophila. *Curr Biol* 19(16):R700–R713.
10. Heisenberg M (2003) Mushroom body memoir: From maps to models. *Nat Rev Neurosci* 4(4):266–275.
11. Butcher NJ, Friedrich AB, Lu Z, Tanimoto H, Meinertzhagen IA (2012) Different classes of input and output neurons reveal new features in microglomeruli of the adult Drosophila mushroom body calyx. *J Comp Neurol* 520(10):2185–2201.
12. Lee T, Lee A, Luo L (1999) Development of the Drosophila mushroom bodies: Sequential generation of three distinct types of neurons from a neuroblast. *Development* 126(18):4065–4076.
13. Honegger KS, Campbell RA, Turner GC (2011) Cellular-resolution population imaging reveals robust sparse coding in the Drosophila mushroom body. *J Neurosci* 31(33): 11772–11785.
14. Wang Y, et al. (2004) Stereotyped odor-evoked activity in the mushroom body of Drosophila revealed by green fluorescent protein-based Ca2+ imaging. *J Neurosci* 24(29):6507–6514.
15. Turner GC, Bazhenov M, Laurent G (2008) Olfactory representations by Drosophila mushroom body neurons. *J Neurophysiol* 99(2):734–746.
16. Wang JW, Wong AM, Flores J, Vosshall LB, Axel R (2003) Two-photon calcium imaging reveals an odor-evoked map of activity in the fly brain. *Cell* 112(2):271–282.
17. Wilson RI, Turner GC, Laurent G (2004) Transformation of olfactory representations in the Drosophila antennal lobe. *Science* 303(5656):366–370.
18. Davis RL (2011) Traces of Drosophila memory. *Neuron* 70(1):8–19.
19. Jortner RA, Farivar SS, Laurent G (2007) A simple connectivity scheme for sparse coding in an olfactory system. *J Neurosci* 27(7):1659–1669.
20. Luo SX, Axel R, Abbott LF (2010) Generating sparse and selective third-order responses in the olfactory system of the fly. *Proc Natl Acad Sci USA* 107(23): 10713–10718.
21. Perez-Orive J, et al. (2002) Oscillations and sparsening of odor representations in the mushroom body. *Science* 297(5580):359–365.
22. Assisi C, Stopfer M, Laurent G, Bazhenov M (2007) Adaptive regulation of sparseness by feedforward inhibition. *Nat Neurosci* 10(9):1176–1184.
23. Demmer H, Kloppenburg P (2009) Intrinsic membrane properties and inhibitory synaptic Input of kenyon cells as mechanisms for sparse coding? *J Neurophysiol* 102(3):1538–1550.
24. Finelli LA, Haney S, Bazhenov M, Stopfer M, Sejnowski TJ (2008) Synaptic learning rules and sparse coding in a model sensory system. *PLOS Comput Biol* 4(4):e1000062.
25. Tian L, et al. (2009) Imaging neural activity in worms, flies and mice with improved GCaMP calcium indicators. *Nat Methods* 6(12):875–881.
26. Zhao Y, et al. (2011) An expanded palette of genetically encoded Ca^{2+} indicators. *Science* 333(6051):1888–1891.
27. Yasuyama K, Meinertzhagen IA, Schürmann FW (2002) Synaptic organization of the mushroom body calyx in Drosophila melanogaster. *J Comp Neurol* 445(3):211–226.
28. Ito K, Awano W, Suzuki K, Hiromi Y, Yamamoto D (1997) The Drosophila mushroom body is a quadruple structure of clonal units each of which contains a virtually identical set of neurones and glial cells. *Development* 124(4):761–771.
29. Aso Y, et al. (2009) The mushroom body of adult Drosophila characterized by GAL4 drivers. *J Neurogenet* 23(1-2):156–172.
30. Potter CJ, Tasic B, Russler EV, Liang L, Luo L (2010) The Q system: A repressible binary system for transgene expression, lineage tracing, and mosaic analysis. *Cell* 141(3): 536–548.
31. Zhu S, Chiang AS, Lee T (2003) Development of the Drosophila mushroom bodies: Elaboration, remodeling and spatial organization of dendrites in the calyx. *Development* 130(12):2603–2610.
32. Knott G, Marchman H, Wall D, Lich B (2008) Serial section scanning electron microscopy of adult brain tissue using focused ion beam milling. *J Neurosci* 28(12): 2959–2964.
33. Jack JJB, Noble D, Tsien RW (1975) *Electric Current Flow in Excitable Cells* (Clarendon Press, Oxford), pp xvi, 502 pp.
34. Trunova S, Baek B, Giniger E (2011) Cdk5 regulates the size of an axon initial segment-like compartment in mushroom body neurons of the Drosophila central brain. *J Neurosci* 31(29):10451–10462.
35. Xu NL, et al. (2012) Nonlinear dendritic integration of sensory and motor input during an active sensing task. *Nature* 492(7428):247–251.
36. Campusano JM, Su H, Jiang SA, Sicaeros B, O'Dowd DK (2007) nAChR-mediated calcium responses and plasticity in Drosophila Kenyon cells. *Dev Neurobiol* 67(11): 1520–1532.
37. Akerboom J, et al. (2012) Optimization of a GCaMP calcium indicator for neural activity imaging. *J Neurosci* 32(40):13819–13840.
38. Gupta N, Stopfer M (2012) Functional analysis of a higher olfactory center, the lateral horn. *J Neurosci* 32(24):8138–8148.
39. Papadopoulou M, Cassenaer S, Nowotny T, Laurent G (2011) Normalization for sparse encoding of odors by a wide-field interneuron. *Science* 332(6030):721–725.
40. Tanaka NK, Tanimoto H, Ito K (2008) Neuronal assemblies of the Drosophila mushroom body. *J Comp Neurol* 508(5):711–755.
41. Olsen SR, Wilson RI (2008) Lateral presynaptic inhibition mediates gain control in an olfactory circuit. *Nature* 452(7190):956–960.
42. Shepherd GM (2004) *The Synaptic Organization of the Brain* (Oxford Univ Press, Oxford), 5th Ed, pp xiv, 719 pp.
43. Shu X, et al. (2011) A genetically encoded tag for correlated light and electron microscopy of intact cells, tissues, and organisms. *PLoS Biol* 9(4):e1001041.
44. Osakada F, et al. (2011) New rabies virus variants for monitoring and manipulating activity and gene expression in defined neural circuits. *Neuron* 71(4):617–631.
45. Wickersham IR, et al. (2007) Monosynaptic restriction of transsynaptic tracing from single, genetically targeted neurons. *Neuron* 53(5):639–647.
46. Grewe BF, Langer D, Kasper H, Kampa BM, Helmchen F (2010) High-speed in vivo calcium imaging reveals neuronal network activity with near-millisecond precision. *Nat Methods* 7(5):399–405.
47. Katona G, et al. (2012) Fast two-photon in vivo imaging with three-dimensional random-access scanning in large tissue volumes. *Nat Methods* 9(2):201–208.